Geophysical Research Letters

RESEARCH LETTER
10.1029/2020GL090735

Wave-Driven Flow Along a Compact Marginal Ice Zone

Jim Thomson[1], Björn Lund[2], John Hargrove[2], Madison M. Smith[1], Jochen Horstmann[3], and Jennifer A. MacKinnon[4]

[1]Applied Physics Laboratory, University of Washington, Seattle, WA, USA, [2]CSTARS, University of Miami, Miami, FL, USA, [3]Helmholtz Zentrum Geesthacht, Geesthacht, Germany, [4]Scripps Institution of Oceanography, UCSD, La Jolla, CA, USA

Key Points:

- Obliquely propagating surface waves drive flow (ice drift) along a marginal ice zone
- Gradients in the waves provide the momentum for the ice drift, which is opposed by ice-ocean stress in a simple model
- Instabilities in the strongly sheared ice drift may cause fluctuations in the ice edge shape

Supporting Information:

- Supporting Information S1
- Movie S1
- Movie S2

Correspondence to:
J. Thomson,
jthomson@apl.washington.edu

Citation:
Thomson, J., Lund, B., Hargrove, J., Smith, M. M., Horstmann, J., & MacKinnon, J. A. (2021). Wave-driven flow along a compact marginal ice zone. *Geophysical Research Letters*, *48*, e2020GL090735. https://doi.org/10.1029/2020GL090735

Received 18 SEP 2020
Accepted 3 JAN 2021

Abstract Observations of surface waves and ice drift along a compact sea ice edge demonstrate the importance of waves in a marginal ice zone. An analytic model is presented for the along-ice drift forced by the radiation stress gradient of oblique waves. A momentum balance using quadratic drag to oppose the wave forcing is sufficient to explain the observations. Lateral shear stresses in the ice are also evaluated, though this balance does not match the observations as well. Additional forcing by local winds is included and is small relative to the wave forcing. However, the wave forcing is isolated to a narrow region around 500-m wide, whereas the wind forcing has effects on larger scales. The simplistic drag is assessed using observations of shear and turbulent dissipation rates. The results have implications for the shape and evolution of the ice edge, because the lateral shear may be a source of instabilities.

Plain Language Summary Ocean surface waves rapidly get smaller when traveling from open water into sea ice. Although waves in sea ice do not break, there are some similarities to waves traveling through the surf zone, which lose most of their energy and momentum before reaching the shore. Here, the wave momentum is transferred to the sea ice and can cause strong ice drift. In the case of waves arriving at an oblique angle to the ice edge, the ice drift is directed along the ice edge, similar to alongshore currents in the surf zone. Continuing the surf-zone analogy, the wave energy is transferred into turbulence below the water (ice) surface. Finally, there are fluctuations in the ice edge shape that may be related to this wave forcing.

1. Introduction

Surface gravity waves carry fluxes of momentum and energy in the direction of propagation. The momentum flux is traditionally termed the "radiation stress" S following the original definition (M. Longuet-Higgins & Stewart, 1964). When waves are dissipated in the marginal ice zone or break in the surf zone, both momentum and energy are released at rates related to the spatial gradients in the waves. There is a need to understand how these wave gradients affect the marginal ice zone, because surface wave heights are increasing in the western Arctic (Li et al., 2019; Q. Liu et al., 2016; Thomson, Fan, et al., 2016; Wang et al., 2015) as a result of increasing open water fetch (Thomson & Rogers, 2014). Surf-zone dynamics provide a useful, though incomplete, analogy in understanding processes driven by strong spatial gradients in wave fluxes.

Previous studies in the marginal ice zone have shown the importance of wave momentum flux for the evolution of a compact ice edge (Martin et al., 1983) and the rafting of ice floes together that can determine ice thickness and extent (Sutherland & Dumont, 2018). More broadly, wave momentum fluxes are known to be important in ice momentum budgets (Hunke & Dukowicz, 1997; A. K. Liu et al., 1993; Steele et al., 1989; Squire, 2007). These previous studies have focused on the wave radiation stress into the marginal ice zone. Few, if any, studies have explored the component of wave radiation stress *along* the marginal ice zone, which becomes significant when waves approach at an oblique angle. Recent modeling work suggests this may be important to ice edge evolution and eddy activity (Dai et al., 2019).

The effects of oblique waves are much more commonly studied in the surf zone, where numerous previous experiments have shown that cross-shore gradients in the flux of wave momentum can drive alongshore currents (Bowen et al., 1968; Feddersen et al., 1998; Lentz et al., 1999; M. S. Longuet-Higgins, 1970). The alongshore currents driven by this mechanism often have significant lateral shear, which has been

shown to generate lateral eddies through a shear instability process (Bowen & Holman, 1989; Oltman-Shay et al., 1989).

The present study uses a unique set of field measurements with oblique waves incident to a marginal ice zone and tests two simple analytic expressions for the transfer of wave momentum into along-ice drift. The results show a clear relation between the wave forcing and the along-ice drift. The discussion explores the dissipation of wave energy as turbulence and uses measurements of turbulent dissipation rates with vertical shear to assess the realism of the analytic models. The conclusions address the general importance of waves in the evolution of the marginal ice zone, including the strong across-ice (lateral) shear in the along-ice motion as a source of instabilities in the ice edge.

2. Analytic Models

An analytic calculation for the momentum flux provides the dynamic balance of oblique wave forcing in the marginal ice zone. An ice-edge coordinate system is applied, with x increasing into the ice ($x = 0$ is the ice edge), y along the ice-edge, and wave angle θ defined relative to the ice-normal direction $\hat{x}$ (i.e., $\theta = 0$ would be waves arriving perpendicular to the ice edge). The wave quantities are vertically integrated and phase-averaged.

The reduction of wave height within the marginal ice is given by the standard attenuation definition,

$$H(x) = H_0 e^{-\alpha x}, \tag{1}$$

where H_0 is the significant wave height incident from open water and α is the attenuation rate. The attenuation rate can be a strong function of frequency (Cheng et al., 2017; Meylan et al., 2014, 2018; Rogers et al., 2016; Wadhams et al., 1988), yet here we choose a bulk α to represent the attenuation over all frequencies. This bulk approach will enable simple analytic expressions for the momentum and energy fluxes that follow; this choice is validated in the Supplemental Information, with an effect on $H(x)$ that is less than 1%. In this usage there is an important distinction between the attenuation, α, that is normal to the ice edge (aligned with x), and the more conventional attenuation, $\alpha\cos(\theta)$, that is aligned along the direction of wave propagation $\frac{x}{\cos(\theta)}$. The α normal to the ice edge is directly related to the component-wise gradients in wave momentum flux, whereas the conventional attenuation is related to the scalar gradient in total wave energy flux. Note also the factor of two difference in attenuation if α were defined in terms of wave energy, $\frac{1}{16}\rho g H^2$, where ρ is the density of seawater and g is gravitational acceleration.

The cross-ice flux of along-ice momentum is given by the xy component of the radiation stress tensor,

$$S_{xy}(x) = \frac{1}{16}\left(\frac{c_g}{c}\right)\rho g H_0^2 e^{-2\alpha x}\sin\theta\cos\theta, \tag{2}$$

Note that in deep water, the ratio of the group velocity to the phase speed is simply $\frac{c_g}{c} = \frac{1}{2}$, assuming wave dispersion is unchanged in thin ice cover without ice flexure or mass loading effects (Collins et al., 2018; A. K. Liu & Mollo-Christensen, 1988; Sutherland & Dumont, 2018). This component S_{xy} is distinct from the cross-ice flux of cross-ice wave momentum S_{xx}, which causes "set-up" in a coastal setting, or the compaction of an ice edge in the marginal ice zone. We focus here on the effects of the along-ice component S_{xy}, because the observed waves are highly oblique (i.e., θ is large).

Assuming spatial homogeneity, the vertically integrated along-ice ($\hat{y}$) momentum balance for a layer of thickness h is (Feddersen et al., 1998; Hunke & Dukowicz, 1997; Lentz et al., 1999)

$$\rho h\frac{DV}{Dt} = -\frac{\partial S_{xy}}{\partial x} + \tau_s - \tau_b - \tau_l \tag{3}$$

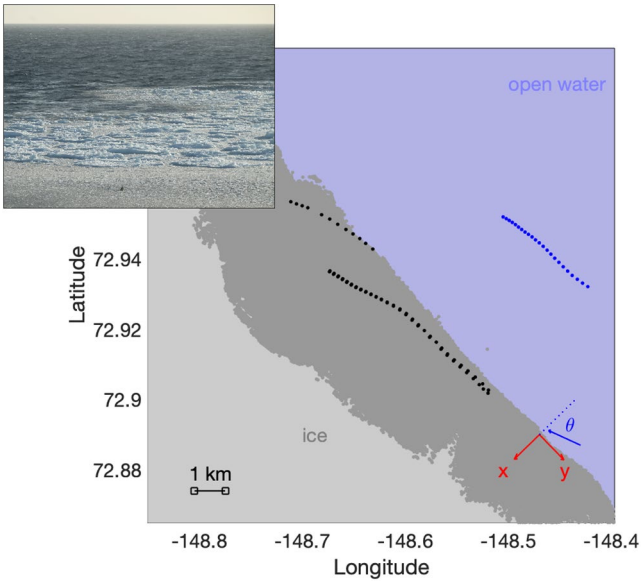

Figure 1. Map of the radar ice mask and buoy positions over the 8-h experiment. The dark gray region is a composite of all ice masks from the shipboard radar. The light gray is the remaining ice (inferred from visual observations). The blue region is open water. The SWIFT locations are shown with circles for every 12-min, drifting toward the northwest (i.e., drifting along the ice edge in y). The fixed x, y coordinate system and wave propagation direction θ are shown in the bottom right corner. The inset photo shows the ice edge as viewed from the bridge of the R/V Sikuliaq, with a SWIFT buoy in the foreground (in the smaller ice floes). Photo by Madison Smith.

This is sometimes termed a "slab" model, because of the vertical integration describing a depth-averaged current $V = \frac{1}{h}\int v(z)dz$. The acceleration on the left-hand side is balanced on the right-hand side by terms representing the gradient of the wave radiation stress, surface stress (from wind), bottom stress (at depth h), and lateral stresses within the layer. The Coriolis term is neglected, given the small spatial scales considered in the observations that follow. In steady state, the left-hand side is zero and terms on the right-hand side must balance.

2.1. Bottom Drag Balance

In both the marginal ice zone and the surf zone, one possible simplification of Equation 3 is a balance between the radiation stress gradient and bottom drag τ_b, neglecting other terms. In the present study of a marginal ice zone, the total water depth is large (~3,000 m) so τ_b represents ice-ocean stresses, instead of an actual bottom stress. Defining a layer depth h for the marginal ice zone is complicated by the composition of the slab itself (which is a mixture of ice and water, even in the case of 100% ice cover, as seen in the photo in Figure 1). Application of Equation 3 to the marginal ice zone considers the slab layer to be a continuous medium with thickness given by the average ice draft and a density similar to seawater ρ. In the present study, h ~1 m.

For the purpose of a simple analytic solution, we consider ice-ocean friction with a quadratic drag,

$$\tau_b = \frac{1}{2}\rho C_D \mid V \mid V, \tag{4}$$

where V is the along-ice drift and C_D is an ice-ocean drag coefficient. Note that this differs from the drag representation commonly used in the surf zone, which is the cross term between the wave orbital velocities $\mid \tilde{u} \mid$ and the depth-average along-shore current $V = \frac{1}{h}\int v(z)dz$ (Feddersen et al., 1998). In the marginal ice zone, the wave orbital velocities are unlikely to be zero at the base of the thin layer, at least for unconsolidated ice floes, and we choose the quadratic drag in V as a bulk representation of momentum losses to frictional drag beneath the ice, form drag of the ice in water, and turbulent Reynolds stresses within the water.

The solution for the along-ice drift when radiation stress balances the quadratic drag is

$$V_b(x) = H_0 e^{-\alpha x}\sqrt{\frac{\alpha g \cos\theta \sin\theta}{8C_D}}. \tag{5}$$

The important point is that the ice drift in Equation 5 decays into the marginal ice zone with the same attenuation rate α as the wave heights in Equation 1. Including a surface wind stress τ_s adds a uniform offset in V that will not vary in x, except for possible changes in the air-ice drag coefficient through the marginal ice zone (which are beyond the scope of the present study). A similar prediction can be made for across-ice drift $U(x)$ using S_{xx}, and that is small for the highly oblique waves considered here.

2.2. Lateral Shear Balance

Another possible simplification of Equation 3 is balance between radiation stress gradient and lateral shear stresses τ_l. Although the ice in the present study is loose brash, this remains a viable limit to the dynamics. The lateral shear stresses can described as:

$$\tau_l = \rho h \frac{\partial}{\partial x}\left(\nu_x \frac{\partial V}{\partial x}\right). \quad (6)$$

For internal ice stresses, ν_x is viscous coefficient, which typically depends on ice thickness, ice strength, and the shear itself (Hunke & Dukowicz, 1997). Equation 6 can also describe turbulent stresses in the water, and then ν_x is an eddy diffusivity. Both are scale-dependent parameters with a large range of values reported in the literature.

The solution for the along-ice drift when radiation stress balances the lateral shear stresses with constant ν_x is

$$V_l(x) = H_0^2 e^{-2\alpha x}\left(\frac{g\cos\theta\sin\theta}{64\nu_x\alpha h}\right). \quad (7)$$

The important point is that the ice drift in Equation 7 decays into the marginal ice zone with *twice* the attenuation rate α as the wave heights in Equation 1 (and thus twice the rate as the other analytic solution for $V(x)$). Again, including a surface wind stress τ_s adds a uniform offset in V that will not vary in x. The decay rate of $V(x)$ is thus a key observable parameter that can be used in distinguishing between the simple models of Equations 5 and 7.

3. Field Methods

Field measurements in a marginal ice zone with oblique waves are used to test the analytic models presented above for the transfer of wave momentum into along-ice drift (Equations 5 and 7). Observations were collected on September 18, 2018 as part of the Stratified Ocean Dynamics in the Arctic (SODA) campaign in the southern portion of the Beaufort Sea, approximately 300 km north of Alaska (USA). Measurements were made from four freely drifting Surface Wave Instrument Floats with Tracking (SWIFT) buoys, as well as a shipboard radar operated on the *R/V Sikuliaq*. Ancillary measurements included winds measured with a shipboard sonic anemometer (Metek uSonic Omni) that was corrected for ship motion (Edson et al., 1998) and visual estimates of ice thickness and floe size. The buoy and radar measurements are analyzed using methods documented previously in the literature, and thus are only briefly reviewed here.

The buoy positions and a composite radar ice map are shown in Figure 1. A movie of these positions is included in Supplemental Information, which shows the ice edge evolution in time. The two (of four total) buoys in the middle of the domain were deployed very close together, which makes their drift tracks difficult to distinguish. Figure 1 also includes a photo of the marginal ice zone, which was comprised of brash ice ranging from large floes (>5 m diameter, >1 m thick) to small floes (<1 m diameter, <0.1 m thick).

Figure 1 shows a local coordinate system, which is rotated 44° from true North to align with the ice edge. As the ice edge fluctuates during the experiment, the radar positions are mapped to both an ice-following coordinate system, x_{ice}, and a fixed coordinate system, x. The rotation (44° from true North) is the same for both coordinate systems, so the difference is simply an offset between the instantaneous ice edge and the time-average ice-edge in the $\hat{x}$ direction. The fluctuating ice edge also has curvature that is not captured in x_{ice}; the net effect of this choice is an $\hat{x}$ direction that is not exactly normal to the instantaneous ice edge but is exactly relative to the wave angle θ and the time-averaged ice edge. These fluctuations are ±10° and do not have a significant effect on the overall results.

3.1. Wave Measurements

Wave measurements from the SWIFT buoys use a combination of Global Position System (GPS) and Inertial Motion Unit (IMU) raw data to estimate the bulk wave parameters of significant wave height H_s, peak wave period T_p, and dominant wave direction θ (here, defined relative to the ice edge), as well as the standard spectral moments as a function of frequency (Herbers et al., 2012; Thomson, 2012; Thomson, Girton, et al., 2018). These SWIFT estimates are produced every 12 min. The four SWIFTs used in this study are version 4 of the SWIFT design (Thomson et al., 2019). The GPS-IMU sensor used in this version is an SBG

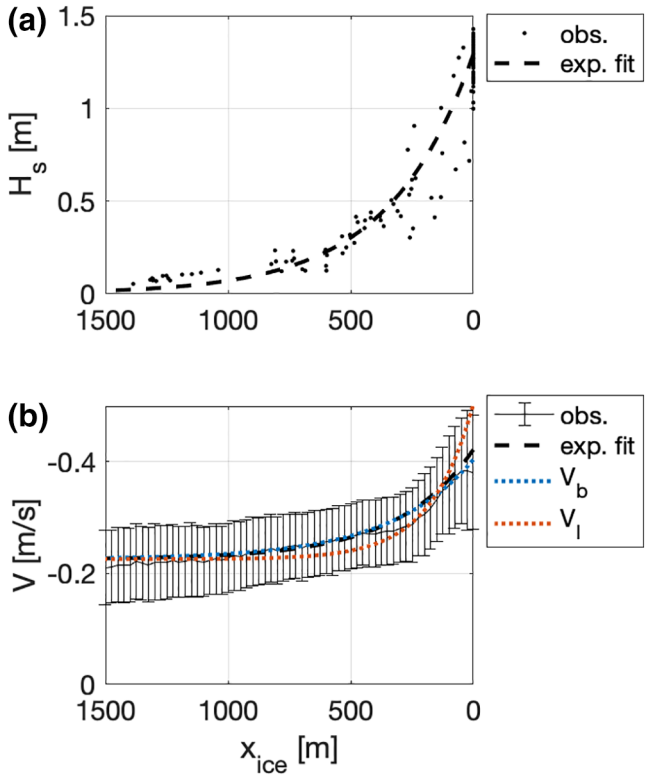

Figure 2. Across-ice dependence of (a) wave heights observed by SWIFTs, and (b) along-ice drift component observed by shipboard radar in bins of $dx = 25$ m. The vertical lines in (b) are the standard deviations of drift values within each distance bin. The bins have approximately 3,000 points each, depending on radar coverage. Both panels include exponential fits to the data (dashed black curves), as reported in Table 1. Panel (b) includes the $V(x)$ predictions from the simple analytic models with quadratic drag (blue curve, Equation 5) and lateral shear (red curve, Equation 7). SWIFT, Surface Wave Instrument Floats with Tracking.

Table 1
Observed and Estimated Parameters, Including Standard Deviations Over the 8 h Experiment and Confidence Intervals

Wind speed	9 ± 1 m/s
Wind direction (rel. to North)	$110 \pm 11°$ (T)
Significant wave height, H_0	1.29 ± 0.06 m
Peak wave period, T_p	6.2 ± 0.8 s
Peak wavelength, λ_p	60 ± 16 m
Peak wave direction (rel. to North), D_p	$112 \pm 9°$ (T)
Wave angle (rel. ice normal), θ	$-67 \pm 9°$
Wave directional spread	$20 \pm 8°$
Ice type	consolidated brash
Ice thickness	0.1–2.0 m
Wave attenuation rate (95% confidence), α	$(2.9 \pm 0.4) \times 10^{-3}$ m^{-1}
Drift attenuation rate (95% confidence)	$(3.2 \pm 0.3) \times 10^{-3}$ m^{-1}
Ice-ocean drag coefficient, C_D	8×10^{-3}
Effective viscosity, ν_x	1×10^2 m^2 s^{-1}

Ellipse N, with raw samples at 5 Hz. Prior versions of these buoys have been used extensively for wave measurements in the marginal ice zone (Cheng et al., 2017; Rogers et al., 2016; Thomson, Ackley, et al., 2018).

3.2. Turbulence Measurements

The version 4 SWIFTs include a downlooking Nortek Signature1000 Acoustic Doppler sonar for vertical profiles of the currents and turbulence. Following existing methods, the current profiles use a broadband mode on the four slanted beams and the turbulence profiles use a pulse-coherent mode on the fifth center beam. The current profiles have 0.5-m resolution from 0.5 to 20.0 m below the surface and are sampled at 1 Hz, then ensemble-averaged to component profiles $u(z)$, $v(z)$ every 12 min. The turbulent profiles have 0.04-m resolution from 0.32 to 2.88 m below the surface and are sampled at 8 Hz, then processed using a spatial structure function to determine a vertical profile of the turbulent dissipation rate $\epsilon(z)$ every 12 min (Thomson, 2012). The structure function results have been shown to agree with the more common estimates using the inertial subrange of turbulent frequency spectra (S. F. Zippel et al., 2018). Previous work has already shown that SWIFT-measured profiles in the sea water between floes can provide meaningful observations of shear and turbulence in the marginal ice zone (Smith & Thomson, 2019; S. Zippel & Thomson, 2016).

3.3. Ice Drift Measurements

Shipboard Helmholtz Zentrum Geesthacht radar (Braun et al., 2008) data are used to form ice masks and estimate ice drift vectors over the approximately 3 km radius of the radar through the use of target detection and optical flow methods (Karvonen, 2016; Mahoney et al., 2015). A similar technique has already been shown to agree well with the drift vectors of buoys in the marginal ice zone (Lund et al., 2018). The radar scans are every 2 s, and the ice products are every 1 min. The effective spatial resolution of the ice masks and ice drift vectors is 50 m. The individual scans and the movie in the Supplemental Information show the time evolution of the ice edge, which has fluctuations of several hundred meters that propagate along the ice. The SWIFT buoy drift velocities and the radar ice drift velocities are well correlated within the marginal ice zone, both in magnitude ($R^2 = 0.8$) and by component ($R^2 = 0.75$).

4. Results

4.1. Observations

The observed conditions and key parameters are summarized in Table 1. Conditions were quasisteady over the 8-h experiment. The observations in Figure 2a show a narrow marginal ice zone, approximately $0 < x_{ice} < 500$ m, in which wave heights are rapidly attenuated. Exponential attenuation (Equation 1) provides a reasonable fit to the observed wave heights. Figure 2b shows the along-ice component of ice drift $V(x)$ measured by the shipboard radar. Exponential attenuation also provides a reasonable fit to these data, with an exponent that is similar to the wave height results (see Table 1). These combined observations suggest a rapid

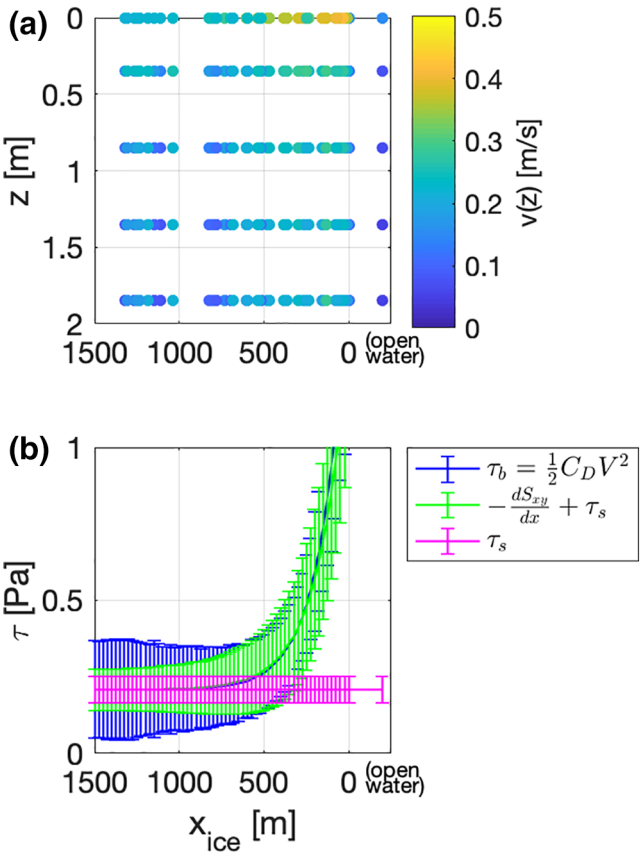

Figure 3. Across-ice dependence of (a) vertical current profiles measured by the SWIFT buoys, (b) select terms in the analytic momentum balance (Equation 3). Both panels include open water values, which are displayed just to the right of $x_{ice} = 0$, but were actually collected 3–4 km from the ice (see Figure 1). The current profiles in (a) are the magnitude of the along-ice component, as indicated with the color scale. Error bars are uncertainties propagated from the fitted decay rates of $V(x)$ and $H(x)$ that are used to calculate the momentum terms. SWIFT, Surface Wave Instrument Floats with Tracking.

transfer of momentum from the waves to the ice in the first 500 m of this marginal ice zone. There is a constant offset of around −0.2 m/s in $V(x)$ estimated as the larger scale drift caused by the wind stress. This "free drift" is approximately 2.5% of the wind speed, which is expected (Zhang et al., 2012) and shown with satellite imagery in the Supplemental Information.

The across-ice drift component is much weaker ($U(x) < 0.1$ m/s), as expected given the oblique waves. This component is shown in the Supplemental Information. It is directed into the ice and thus likely still important to forming a compact ice edge and consolidated marginal ice zone.

4.2. Assessment of the Analytic Models

Figure 2b suggests that both simple expressions for the along-ice drift are reasonable, so long as a constant offset from wind drift of ∼0.2 m/s is applied. The solution using quadratic drag (blue curve, Equation 5) is a better match to the observations than the solution using lateral shear stress (red curve, Equation 7). The fitted decay of $V(x)$ is similar to the decay of $H(x)$, as given by Equation 5, rather than twice the decay of $H(x)$, as given by Equation 7. A more comprehensive solution would include both the drag and shear terms simultaneously in the momentum balance (Equation 3), which would provide sufficient degrees of freedom to improve an empirical fit to $V(x)$. We leave this fitting exercise as future work, and instead proceed to understand the details of the drag term.

The quadratic drag model assumes a thin slab that is moving relative to still water below. If the water below was not still, there would be an offset velocity in the quadratic drag law, which can even change the sign of the ice-ocean stress in some cases (Lu et al., 2011). v 3a shows the vertical profiles of the along-ice motion $v(z)$, which support this assumption with observations of strong shear between the surface drift and the values below. The profiles shown span the range of visual ice thickness estimates (0.1–2 m). The velocity profiles have been adjusted from the wave-following reference frame to a sea-level reference frame, including the Stokes shear (Amador et al., 2017; Thomson et al., 2019). The figure includes an ensemble average profile from the SWIFT in open water, which lacks the strong shear that is observed within the ice.

Figure 3b shows select terms of the momentum balance (Equation 3), in which the combination of wave radiation stress gradient and surface wind stress are approximately in balance with the drag term τ_b. The stress τ_b is estimated using the fitted $V(x)$ from observations and a drag coefficient of $C_D = 8 \times 10^{-3}$, which is within the range of recent literature on ice-ocean drag (Tsamados et al., 2014). The wave radiation stress gradient is estimated using the fitted $H(x)$ from observations. The surface stress τ_s is estimated using an inertial dissipation estimate (Yelland et al., 1994) based on turbulent wind measurements in the ice and in open water. Bulk estimates for the magnitude of forcing terms give a wave radiation stress gradient of 0.7 Pa and a wind stress of 0.2 Pa, which are aligned at similar oblique angles to the ice edge. Thus, the waves impart significantly more momentum to the ice, but only in a narrow region that is localized by the gradients in the waves themselves.

5. Discussion

Here we discuss alternate forms of the stress τ_b, including how vertical mixing in the water column might provide the stress necessary to balance the wave momentum, as well as how the form drag of the ice floes might dissipate the wave energy as turbulence. Our focus is on the turbulence implied by τ_b, but we note

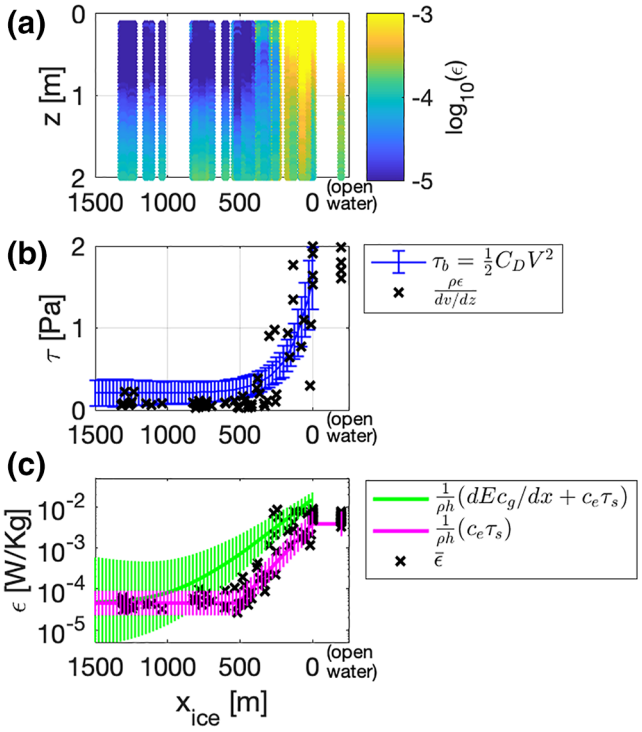

Figure 4. Across-ice dependence of (a) turbulent dissipation rate profiles measured by the SWIFT buoys, (b) bottom stress estimates if turbulent dissipation balances shear production at the base of the slab, and (c) turbulent dissipation rates predicted by the combined wave and wind forcing (green curve), as well as for the wind alone (magenta curve), following Equation 10. Both panels include open water values, which are displayed just to the right of $x_{ice} = 0$, but were actually collected 3–4 km from the ice (see Figure 1). Error bars are uncertainties propagated from the fitted decay rates of $V(x)$ and $H(x)$ that are used to calculate the terms. SWIFT, Surface Wave Instrument Floats with Tracking.

that the lateral ice-ice stresses τ_l evaluated earlier also may be important. We simply lack any direct observations to explore those ice-ice stresses.

Vertical profiles of the turbulent dissipation rate estimated from the SWIFT buoys are shown in Figure 4a. Near the ice edge ($0 < x_{ice} < 250$ m), the turbulent dissipation rates exceed 10^{-3} W/kg in the surface layer. Such large rates of dissipation are typically only observed in the crests of breaking waves (Gemmrich, 2010; Sutherland & Melville, 2015; Thomson, Schwendeman, et al., 2016). Indeed, similar dissipation rates are observed in open water during this study, where 9 m/s winds cause whitecaps to form at the ocean surface. Within the marginal ice zone, the whitecaps are suppressed (see picture in Figure 1) and other processes must be causing the high dissipation rates. Farther into the marginal ice zone, the near-surface dissipation rates are below 10^{-5} W/kg, coincident with reduced wave heights, while the deeper dissipation rates remain 10^{-4} W/kg. These observations suggest that surface wave forcing is important near the ice-edge and subsurface shear is important farther within the ice.

5.1. Vertical Shear and Mixing

The stress term τ_b from Equation 3 can be recast as a vertical mixing term representing Reynolds stresses within the water column,

$$\tau_b \approx \rho \int \frac{\partial}{\partial z}\left(\nu_{tz}\frac{\partial v}{\partial z}\right)dz, \tag{8}$$

instead of the quadratic form in Equation 4. An analytic solution using this as the sole sink of momentum can predict ice drifts of $V \sim 0.5$ m/s using a constant vertical eddy viscosity $\nu_{tz} = 10^{-3}$. However, this solution predicts a $V(x)$ that decays twice as fast with distance into the ice (just as the lateral shear solution does in Equation 7), which is not consistent with the observations (Figure 2). Furthermore, this approach requires specification of the vertical shear $v(z)$ through the marginal ice zone, which is rarely available from observations.

The observations in the present study are suitable to assess the classic balance of turbulent production via shear $\tau_b \dfrac{dv}{dz}$ with the dissipation rate $\epsilon(z)$, such as might occur at the base of the layer (where vertical shear is maximum). The balance of those observed quantities provides independent estimates of the stress,

$$\tau_b \approx \frac{\rho\epsilon(z)}{dv\ /\ dz}, \tag{9}$$

which are shown in Figure 4b. The estimates show some agreement, though there is considerable scatter. There appears to be an excess of dissipation near the ice edge, perhaps related to additional production of turbulence by the form drag of ice floes in the active wavefield. Farther into the marginal ice zone, there appears be insufficient dissipation. In open water, the balance in Equation 9 is not expected to be valid near the surface, because turbulence is produced by whitecaps instead of by mean shear (Gemmrich, 2010; Sutherland & Melville, 2015; Thomson, Schwendeman, et al., 2016).

It could be that density gradients in the marginal ice zone are important to the turbulent dynamics. A buoyancy term would alter the balance of shear production and dissipation in Equation 9, with a general effect of stabilizing the interface. Following Smith and Thomson (2019), we estimate that this effect is small, though it is not well-constrained.

5.2. Wave Energy and Turbulent Dissipation

Recent work suggests that the motion of ice floes in a wavefield attenuates wave energy via turbulence in the water (Voermans et al., 2019), and thus wave measurements can provide an independent estimate for comparison with the observed turbulent dissipation rates. The rate of wave energy loss is given by the spatial gradient in the wave energy flux $\frac{1}{16}\rho g c_g H^2$ along the direction of wave propagation. Using the wave heights in Equation 1, the gradient $\frac{\partial}{\partial x}$ in energy flux $\frac{1}{16}\rho g c_g H^2$ becomes an estimate of depth-average turbulent dissipation rate within the active layer

$$\bar{\epsilon} = \frac{1}{\rho h}\left(\frac{1}{8}\rho g c_g \alpha \cos(\theta) H_0^2 e^{-2\alpha x} + c_e \tau_s\right) \tag{10}$$

A second term is included on the right-hand-side to represent the direct flux of turbulent energy from the wind, which would be a local source of turbulence unrelated to the wave gradient. This is estimated using an effective transfer speed c_e, which transitions smoothly from the wave phase speed in open water to the ice drift speed far within the marginal ice zone (Smith & Thomson, 2019; S. Zippel & Thomson, 2016).

Figure 4c compares the expected turbulent dissipation rates (Equation 10) with the depth-average $\bar{\epsilon}$ from SWIFT measurements. Near the ice edge ($0 < x_{\text{ice}} < 300$), the observed $\bar{\epsilon}$ are similar to the predictions. Farther in the ice ($x_{\text{ice}} > 300$), the observed $\bar{\epsilon}$ are insufficient to match the predictions, and this suggests that wave energy must also be lost by other mechanisms, such as ice collisions and flexure. The overall implication is that the turbulence near the ice edge is mostly generated by wave motions stirring the ice floes and that turbulence farther within the ice is generated by wind work and mean shear.

6. Conclusions

A simple quadratic drag model for ice drift forced by obliquely incident waves successfully explains observations in a marginal ice zone. The key feature is strong lateral shear in the along-ice component of drift, which matches the gradient of the wave radiation stress within the marginal ice zone. The value of the ice-ocean drag coefficient likely is related to the specific mixture of small brash ice floes and seawater in the near-surface layer. Indeed, it is probably the lack of a continuous ice sheet that allows such strong lateral shear in $V(x)$ to be sustained without lateral stresses in the ice dominating the dynamics.

The intense lateral shear near the ice edge may be a source of instabilities causing fluctuations in the ice edge shape. The radar ice movies in the Supplemental Information have features that clearly propagate along the ice edge, with a standard deviation of the instantaneous ice edge position relative to mean position that is $L_x = 262$ m. This distance is about half of the e-folding scale for the wave attenuation $\alpha^{-1} = 419$ m, and this is qualitatively consistent with the conventional view that the fastest growing mode of a shear instability will have a wavelength similar to the length scale for the shear itself (Vallis, 2017). The overall concept is a wave attenuation rate that sets the scale of the shear and along-ice drift, which sets the scale of subsequent shear instabilities. Vorticity analysis in the Supplemental Information also is consistent with significant activity on scales of L_x. This may be an important, and previously unexplored, mechanism controlling ice edge morphology on small scales (i.e., <1 km).

Acknowledgments
This work was supported by the Office of Naval Research (Award N00014-16-1-2349). Alex de Klerk and Joe Talbert built and prepared the SWIFT buoys. Erik Dahl assisted with the deployments. The captain and crew of the *R/V Sikuliaq* provided comprehensive logistical, operational, and scientific support. Jan Bödewadt, Neil Williams, Ethan Roth, and Cris Seaton assisted with the radar operations. Jérémy Baudry, Dany Dumont, and two anonymous reviewers provide valuable comments on the manuscript.

Data Availability Statement

Data are available in the public archive at the University of Washington Digital Library collection: http://hdl.handle.net/1773/46602

References

Amador, A., Jaramillo, S., & Pawlak, G. (2017). Adcp bias and stokes drift in auv-based velocity measurements. *Journal of Atmospheric and Oceanic Technology*, *34*(9), 2029–2042. https://doi.org/10.1175/JTECH-D-16-0182.1

Bowen, A. J., & Holman, R. A. (1989). Shear instabilities of the mean longshore current: 1. theory. *Journal of Geophysical Research*, *94*(C12), 18023–18030. https://doi.org/10.1029/JC094iC12p18023 Retrieved from https://agupubs.onlinelibrary.wiley.com/doi/abs/10.1029/JC094iC12p18023

Bowen, A. J., Inman, D. L., & Simmons, V. P. (1968). Wave 'set-down' and set-up. *Journal of Geophysical Research*, *73*(8), 2569–2577. https://doi.org/10.1029/JB073i008p02569 Retrieved from https://agupubs.onlinelibrary.wiley.com/doi/abs/10.1029/JB073i008p02569

Braun, N., Ziemer, F., Bezuglov, A., Cysewski, M., & Schymura, G. (2008). Sea-surface current features observed by doppler radar. *IEEE Transactions on Geoscience and Remote Sensing*, *46*(4), 1125–1133.

Cheng, S., Rogers, W. E., Thomson, J., Smith, M., Doble, M. J., Wadhams, P., et al. (2017). Calibrating a viscoelastic sea ice model for wave propagation in the arctic fall marginal ice zone. *Journal of Geophysical Research: Oceans*, *122*, 8770–8793. https://doi.org/10.1002/2017JC013275

Collins, C. O., Doble, M., Lund, B., & Smith, M. (2018). Observations of surface wave dispersion in the marginal ice zone. *Journal of Geophysical Research: Oceans*, *123*(5), 3336–3354. https://doi.org/10.1029/2018JC013788 Retrieved from https://agupubs.onlinelibrary.wiley.com/doi/abs/10.1029/2018JC013788

Dai, H.-J., McWilliams, J. C., & Liang, J.-H. (2019). Wave-driven mesoscale currents in a marginal ice zone. *Ocean Modelling*, *134*, 1–17. https://doi.org/10.1016/j.ocemod.2018.11.006 Retrieved from http://www.sciencedirect.com/science/article/pii/S1463500318303810

Edson, J. B., Hinton, A. A., Prada, K. E., Hare, J. E., & Fairall, C. W. (1998). Direct covariance flux estimates from mobile platforms at sea*. *Journal of Atmospheric and Oceanic Technology*, *15*(2), 547–562. https://doi.org/10.1175/1520-0426(1998)015<0547:DCFEFM>2.0.CO;2

Feddersen, F., Guza, R. T., Elgar, S., & Herbers, T. H. C. (1998). Alongshore momentum balances in the nearshore. *Journal of Geophysical Research*, *103*(C8), 15667–15676. https://doi.org/10.1029/98JC01270 Retrieved from https://agupubs.onlinelibrary.wiley.com/doi/abs/10.1029/98JC01270

Gemmrich, J. (2010). Strong turbulence in the wave crest region. *Journal of Physical Oceanography*, *40*, 583–595. https://doi.org/10.1175/2009JPO4179.1

Herbers, T. H. C., Jessen, P. F., Janssen, T. T., Colbert, D. B., & MacMahan, J. H. (2012). Observing ocean surface waves with GPS tracked buoys. *Journal of Atmospheric and Oceanic Technology*, *29*, 944–959. https://doi.org/10.1175/JTECH-D-11-00128.1

Hunke, E. C., & Dukowicz, J. K. (1997). An elastic-viscous-plastic model for sea ice dynamics. *Journal of Physical Oceanography*, *27*(9), 1849–1867. https://doi.org/10.1175/1520-0485(1997)027<1849:AEVPMF>2.0.CO;2

Karvonen, J. (2016). Virtual radar ice buoys—A method for measuring fine-scale sea ice drift. *The Cryosphere*, *10*(1), 29–42. https://doi.org/10.5194/tc-10-29-2016 Retrieved from https://www.the-cryosphere.net/10/29/2016/

Lentz, S., Guza, R. T., Elgar, S., Feddersen, F., & Herbers, T. H. C. (1999). Momentum balances on the North Carolina inner shelf. *Journal of Geophysical Research*, *104*(C8), 18205–18226.

Li, J., Ma, Y., Liu, Q., Zhang, W., & Guan, C. (2019). Growth of wave height with retreating ice cover in the arctic. *Cold Regions Science and Technology*, *164*, 102790. https://doi.org/10.1016/j.coldregions.2019.102790 Retrieved from http://www.sciencedirect.com/science/article/pii/S0165232X19300394

Liu, Q., Babanin, A. V., Zieger, S., Young, I. R., & Guan, C. (2016). Wind and wave climate in the arctic ocean as observed by altimeters. *Journal of Climate*, *29*(22), 7957–7975. https://doi.org/10.1175/JCLI-D-16-0219.1

Liu, A. K., Häkkinen, S., & Peng, C. Y. (1993). Wave effects on ocean-ice interaction in the marginal ice zone. *Journal of Geophysical Research*, *98*(C6), 10025–10036. https://doi.org/10.1029/93JC00653 Retrieved from https://agupubs.onlinelibrary.wiley.com/doi/abs/10.1029/93JC00653

Liu, A. K., & Mollo-Christensen, E. (1988). Wave propagation in a solid ice pack. *Journal of Physical Oceanography*, *18*(11), 1702–1712.

Longuet-Higgins, M. S. (1970). Longshore currents generated by obliquely incident sea waves: 2. *Journal of Geophysical Research*, *75*(33), 6790–6801. https://doi.org/10.1029/JC075i033p06790 Retrieved from https://agupubs.onlinelibrary.wiley.com/doi/abs/10.1029/JC075i033p06790

Longuet-Higgins, M., & Stewart, R. (1964). Radiation stresses in water waves; a physical discussion, with applications. *Deep-Sea Research and Oceanographic Abstracts*, *11*(4), 529–562. https://doi.org/10.1016/0011-7471(64)90001-4 Retrieved from http://www.sciencedirect.com/science/article/pii/0011747164900014

Lu, P., Li, Z., Cheng, B., & Leppäranta, M. (2011). A parameterization of the ice-ocean drag coefficient. *Journal of Geophysical Research*, *116*(C7). https://doi.org/10.1029/2010JC006878 Retrieved from https://agupubs.onlinelibrary.wiley.com/doi/pdf/10.1029/2010JC006878

Lund, B., Graber, H. C., Persson, P. O. G., Smith, M., Doble, M., Thomson, J., & Wadhams, P. (2018). Arctic sea ice drift measured by shipboard marine radar. *Journal of Geophysical Research: Oceans*, *123*, 4298–4321. https://doi.org/10.1029/2018JC013769 Retrieved from https://agupubs.onlinelibrary.wiley.com/doi/abs/10.1029/2018JC013769

Mahoney, A. R., Eicken, H., Fukamachi, Y., Ohshima, K. I., Simizu, D., Kambhamettu, C., et al. (2015). Taking a look at both sides of the ice: Comparison of ice thickness and drift speed as observed from moored, airborne and shore-based instruments near barrow, Alaska. *Annals of Glaciology*, *56*(69), 363–372. https://doi.org/10.3189/2015AoG69A565 Retrieved from https://www.cambridge.org/core/article/taking-a-look-at-both-sides-of-the-ice-comparison-of-ice-thickness-and-drift-speed-as-observed-from-moored-airborne-and-shorebased-instruments-near-barrow-alaska/E92D41BCCB9A96C9CCB484E335365F54

Martin, S., Kauffman, P., & Parkinson, C. (1983). The movement and decay of ice edge bands in the winter bering sea. *Journal of Geophysical Research*, *88*(C5), 2803–2812. https://doi.org/10.1029/JC088iC05p02803 Retrieved from https://agupubs.onlinelibrary.wiley.com/doi/abs/10.1029/JC088iC05p02803

Meylan, M. H., Bennetts, L. G., & Kohout, A. L. (2014). In situ measurements and analysis of ocean waves in the Antarctic marginal ice zone. *Geophysical Research Letters*, *41*(14), 5046–5051. https://doi.org/10.1002/2014GL060809

Meylan, M. H., Bennetts, L. G., Mosig, J. E. M., Rogers, W. E., Doble, M. J., & Peter, M. A. (2018). Dispersion relations, power laws, and energy loss for waves in the marginal ice zone. *Journal of Geophysical Research: Oceans*, *123*(5), 3322–3335. https://doi.org/10.1002/2018JC013776 Retrieved from https://agupubs.onlinelibrary.wiley.com/doi/abs/10.1002/2018JC013776

Oltman-Shay, J., Howd, P. A., & Birkemeier, W. A. (1989). Shear instabilities of the mean longshore current: 2. Field observations. *Journal of Geophysical Research*, *94*(C12), 18031–18042. https://doi.org/10.1029/JC094iC12p18031 Retrieved from https://agupubs.onlinelibrary.wiley.com/doi/abs/10.1029/JC094iC12p18031

Rogers, W. E., Thomson, J., Shen, H. H., Doble, M. J., Wadhams, P., & Cheng, S. (2016). Dissipation of wind waves by pancake and frazil ice in the autumn Beaufort Sea. *Journal of Geophysical Research: Oceans*, *121*(11), 7991–8007. https://doi.org/10.1002/2016JC012251

Smith, M., & Thomson, J. (2019). Ocean surface turbulence in newly formed marginal ice zones. *Journal of Geophysical Research: Oceans*, *124*(3), 1382–1398. https://doi.org/10.1029/2018JC014405

Squire, V. A. (2007). Of ocean waves and sea ice revisited. *Cold Regions Science and Technology*, *49*, 110–133.

Steele, M., Morison, J. H., & Untersteiner, N. (1989). The partition of air-ice-ocean momentum exchange as a function of ice concentration, floe size, and draft. *Journal of Geophysical Research*, *94*, 12739–12750.

Sutherland, P., & Dumont, D. (2018). Marginal ice zone thickness and extent due to wave radiation stress. *Journal of Physical Oceanography*, *48*, 1885–1901. https://doi.org/10.1175/JPO-D-17-0167.1

Sutherland, P., & Melville, W. K. (2015). Field measurements of surface and near-surface turbulence in the presence of breaking waves. *Journal of Physical Oceanography*, *45*(4), 943–965. https://doi.org/10.1175/JPO-D-14-0133.1

Thomson, J. (2012). Wave breaking dissipation observed with SWIFT drifters. *Journal of Atmospheric and Oceanic Technology*, *29*(12), 1866–1882. https://doi.org/10.1175/JTECH-D-12-00018.1

Thomson, J., Ackley, S., Girard-Ardhuin, F., Ardhuin, F., Babanin, A., Boutin, G., et al. (2018). Overview of the arctic sea state and boundary layer physics program. *Journal of Geophysical Research: Oceans*, *123*(12), 8674–8687. https://doi.org/10.1002/2018JC013766 Retrieved from https://agupubs.onlinelibrary.wiley.com/doi/abs/10.1002/2018JC013766

Thomson, J., Fan, Y., Stammerjohn, S., Stopa, J., Rogers, W. E., Girard-Ardhuin, F., et al. (2016). Emerging trends in the sea state of the Beaufort and Chukchi seas. *Ocean Modelling*, *105*, 1–12. http://dx.doi.org/10.1016/j.ocemod Retrieved from http://www.sciencedirect.com/science/article/pii/S1463500316300622

Thomson, J., Girton, J. B., Jha, R., & Trapani, A. (2018). Measurements of directional wave spectra and wind stress from a wave glider autonomous surface vehicle. *Journal of Atmospheric and Oceanic Technology*, *35*(2), 347–363. https://doi.org/10.1175/JTECH-D-17-0091.1

Thomson, J., Moulton, M., de Klerk, A., Talbert, J., Guerra, M., Kastner, S., et al. (2019). A new version of the swift platform for waves, currents, and turbulence in the ocean surface layer. In M. Heron & H. Roarty (Eds.), *EEE/OES workshop on currents, waves, and turbulence measurements*. (pp. 1–7). IEEE.

Thomson, J., & Rogers, W. E. (2014). Swell and sea in the emerging Arctic Ocean. *Geophysical Research Letters*, *41*(9), 3136–3140. https://doi.org/10.1002/2014GL059983

Thomson, J., Schwendeman, M. S., Zippel, S. F., Moghimi, S., Gemmrich, J., & Rogers, W. E. (2016). Wave-breaking turbulence in the ocean surface layer. *Journal of Physical Oceanography*, *46*(6), 1857–1870. https://doi.org/10.1175/JPO-D-15-0130.1

Tsamados, M., Feltham, D. L., Schroeder, D., Flocco, D., Farrell, S. L., Kurtz, N., et al. (2014). Impact of variable atmospheric and oceanic form drag on simulations of arctic sea ice. *Journal of Physical Oceanography*, *44*(5), 1329–1353. https://doi.org/10.1175/JPO-D-13-0215.1

Vallis, G. K. (2017). *Atmospheric and oceanic fluid dynamics*. Cambridge, UK: Cambridge University Press.

Voermans, J. J., Babanin, A. V., Thomson, J., Smith, M. M., & Shen, H. H. (2019). Wave attenuation by sea ice turbulence. *Geophysical Research Letters*, *46*(12), 6796–6803. https://doi.org/10.1029/2019GL082945 Retrieved from https://agupubs.onlinelibrary.wiley.com/doi/abs/10.1029/2019GL082945

Wadhams, P., Squire, V. A., Goodman, D. J., Cowan, A. M., & Moore, S. C. (1988). The attenuation rates of ocean waves in the marginal ice zone. *Journal of Geophysical Research*, *93*(C6), 6799–6818.

Wang, X. L., Feng, Y., Swail, V. R., & Cox, A. (2015). Historical changes in the Beaufort-Chukchi-Bering seas surface winds and waves, 1971-2013. *Journal of Climate*, *28*(19), 7457–7469. https://doi.org/10.1175/JCLI-D-15-0190.1

Yelland, M., Taylor, P., Consterdine, I., & Smith, M. (1994). The use of the inertial dissipation technique for shipboard wind stress determination. *Journal of Atmospheric and Oceanic Technology*, *11*, 1093–1108.

Zhang, J., Lindsay, R., Schweiger, A., & Rigor, I. (2012). Recent changes in the dynamic properties of declining arctic sea ice: A model study. *Geophysical Research Letters*, *39*(20). https://doi.org/10.1029/2012GL053545 Retrieved from https://agupubs.onlinelibrary.wiley.com/doi/abs/10.1029/2012GL053545

Zippel, S., & Thomson, J. (2016). Air-sea interactions in the marginal ice zone. *Elementa Science of the Anthropocene*, *4*, 000095.

Zippel, S. F., Thomson, J., & Farquharson, G. (2018). Turbulence from breaking surface waves at a river mouth. *Journal of Physical Oceanography*, *48*(2), 435–453. https://doi.org/10.1175/JPO-D-17-0122.1